




Disclination states in nonreciprocal topological networks

Haoye Qin, Zhe Zhang , Qiaolu Chen, and Romain Fleury 

Laboratory of Wave Engineering, School of Electrical Engineering, EPFL, 1015 Lausanne, Switzerland

 (Received 6 April 2023; revised 27 November 2023; accepted 4 December 2023; published 10 January 2024)

Recently, nonreciprocal two-dimensional unitary scattering networks have gained considerable interest due to the possibility of obtaining robust edge wave propagation in their anomalous topological insulating phase. However, zero-dimensional states in such networks have been left uncharted. Here, we demonstrate the existence of disclination states in nonreciprocal topological scattering networks. The disclination states can nucleate in every gap of the anomalous phase if a disclination round-trip resonance condition is met, and are carried over to the Chern phase unless the band gap closes. By comparing Chern and anomalous disclination states, we show that only the latter are remarkably robust to random quasienergy fluctuations. Anomalous topological chiral edge states and disclinations can be coupled together to form intriguing disclination bound states in the continuum (BICs) in anomalous topological insulators, a different form of nonreciprocal cavities associated with an extreme confinement and lifetime. Our work broadens the applications of disclination states to microwave, acoustic, or optical scattering networks, with new possibilities in chiral topological lasing, robust nonreciprocal energy squeezing, and switchable lasing and antilasing behavior.

DOI: [10.1103/PhysRevResearch.6.013031](https://doi.org/10.1103/PhysRevResearch.6.013031)

I. INTRODUCTION

Two-dimensional (2D) topological insulators are one of the simplest and practically relevant forms of topological systems due to their compatibility with modern planar technologies and fabrication methods in electronics, photonics, and phononics. They exhibit chiral or helical edge transport that originates from bulk-boundary correspondence, a property guaranteed by a quantized number known as bulk topological invariant [1,2]. Topological edge states have been realized in various platforms ranging from quantum to classical waves, including photonic and acoustic lattices [3–6]. In systems with broken time-reversal symmetry, Chern edge states have been observed and exploited for unidirectional wave routing and robust transport of energy [7–10]. However, they are not the only possible 2D chiral edge states. In unitary (e.g., Floquet) systems, for which the spectrum lives in a compact space, an extra anomalous topological phase exists, with zero Chern numbers for all bands, and an equal number of chiral edge states in each gap [11–14]. While the topology of unitary systems is now well understood [11,15,16], photonic anomalous phases have been only recently implemented, in both reciprocal [17–20] and nonreciprocal [14,21,22] systems. Surprisingly, anomalous edge transport was found to be much more resilient than Chern edge transport to various types of distributed perturbations, including arbitrarily large quasienergy fluctuations, scattering matrix disorder, and strong amorphism [21,22].

These years have also witnessed discoveries of higher-order topological states in topological insulators, such as

zero-dimensional (0D) corner, dislocation or disclination states in 2D insulators [6,23–36], as well as hinge and corner states in three-dimensional (3D) insulators [37,38]. Similar to topological edge-mode lasers [39–43], these 0D higher-order states lead to robust field trapping with stronger localization than one-dimensional (1D) edge modes, enabling low-threshold topological lasing at corners [44,45]. Albeit disclination states have been extensively studied in topological crystalline insulators protected by time-reversal symmetry (TRS), disclination states in TRS-breaking systems, including unitary scattering networks supporting the anomalous and Chern phases, still remain largely unexplored.

Here, we unveil the existence of 0D states localized at disclinations in topological nonreciprocal scattering networks, composed of interconnected unitary circulators. Starting from a hexagonal lattice, a simple cut-and-glue procedure leads to 0D disclination states that can nucleate in every band gap in the anomalous phase, together with the 1D edge states. The connection between disclination modes and topological edge states is discussed. The occurrence of the disclination states at the phase-rotation symmetry points can be understood from a round-trip resonance condition of a topological edge state and described by disclination charges. Remarkably, the disclination states can be carried over to the Chern phase, unless the gap closes. We demonstrate the superior robustness of the disclination states occurring in the anomalous phase over the ones occurring in the Chern phase, and exploit their coupling with anomalous edge states to create a different form of disclination bound states in the continuum (BICs), opening intriguing possibilities in electromagnetic energy squeezing and lasing.

II. EMERGENCE OF DISCLINATION STATES

In Fig. 1(a), we consider a hexagonal nonreciprocal scattering network where each scattering node is a clockwise

Published by the American Physical Society under the terms of the [Creative Commons Attribution 4.0 International](https://creativecommons.org/licenses/by/4.0/) license. Further distribution of this work must maintain attribution to the author(s) and the published article's title, journal citation, and DOI.

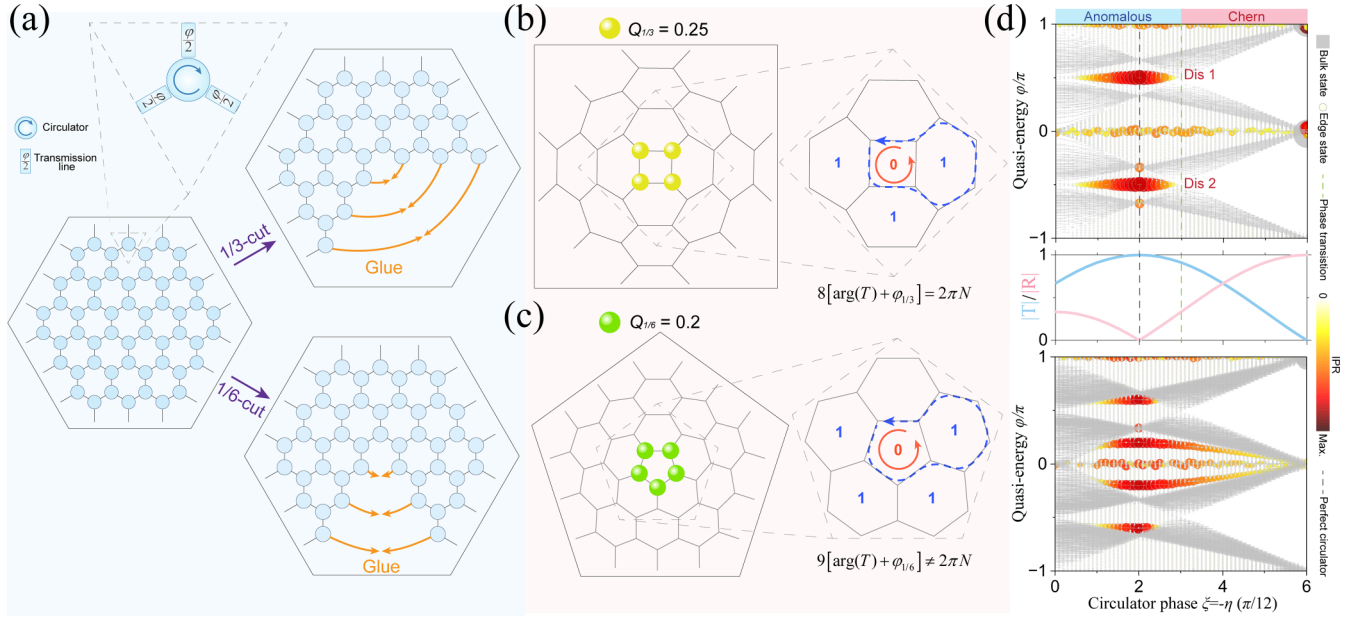


FIG. 1. Disclination states in nonreciprocal scattering networks. (a) Initial hexagonal network of circulators connected through transmission lines (TLs) with a phase delay φ , and cut-and-glue method for generating disclinations. (b),(c) Disclination networks of (b) 1/3-cut and (c) 1/6-cut with distinct spectral charges (colored dots). The zoomed-in view of the center shows the principal disclination loop “0” and surrounding higher-order loops “1.” (d) Evolution of the quasienergy band structure for the networks in (b) (top) and (c) (bottom) vs the circulator parameters R, T , plotted in the middle, which are controlled by a single circulator phase parameter. The color and size of each scatterer indicate the mode’s inverse participation ratio (IPR), from gray (bulk states) and light yellow (edge states) to red (disclination states).

circulator and each link is a monomode transmission line (TL) imparting a phase delay φ . The unitary scattering matrix of such circulators is $S_c = [R, T, D; D, R, T; T, D, R]$, where T and D are clockwise and counterclockwise complex transmission coefficients, respectively. Note that we assume a C3-symmetric model for S_c . The unitary parametrization of S_c involves two independent phase parameters, η and ξ , which control the reflection R and nonreciprocity T/D (see Appendices). Insulating phases in this lattice can then be classified as being either trivial, anomalous, or of Chern type [15,16,21]. The Chern phase, as usual, has nontrivial Chern numbers that must add up to zero for all bands, thus exhibiting both trivial and topological band gaps. In contrast, the anomalous phase, with vanishing Chern numbers for all bands, hosts a topological edge mode for every gap, dictated by a homotopy gap invariant W [16].

For didactic purposes, here we use a single parameter $\xi = -\eta$, which is sufficient to go from the anomalous phase ($0 < \eta < \pi/4$) to the Chern phase ($\pi/4 < \eta < \pi/2$) (see Appendices). We now create disclination defects in such a system. Following a cut-and-glue method (Fig. 1(a)), a 1/3 (or 1/6) portion of the hexagon is first removed, before connecting the remaining TLs, keeping constant all phase delays in the network. With perfect circulators ($R = 0, |T| = 1, \xi = -\eta = \pi/6$), chiral waves propagating along the disclination loop [loop “0” in Figs. 1(b) and 1(c)] are completely isolated from the surrounding loops, and the existence condition for a disclination state is the one of constructive self-interference after a round trip. Concretely, the quasienergy $\varphi_{1/k}$ required for a $1/k$ -cut disclination state is (see Appendices)

$$n_k [\arg(T) + \varphi_{1/k}] = 2\pi N, \quad (1)$$

where $n_k = 6(1 - 1/k)$ is the number of sides of the loop “0,” $T = -1$ is the transmission coefficient of perfect circulators, and N is an integer. This leads to $\varphi_{1/3} = \pm 0.5\pi$ and $\varphi_{1/6} = \pm 0.2\pi, \pm 0.6\pi$. We calculated the disclination spectral charge [25] for each site to be $Q_{1/3} = 0.25$ in Fig. 1(b) and $Q_{1/6} = 0.2$ in Fig. 1(c). Summation of the charge over the four or five disclination sites always yields 1. Incidentally, the condition $R = 0$ is known as a phase-rotation symmetry point [16], which occurs in the anomalous phase. Therefore, the condition (1) is always associated with the anomalous network of perfect circulators, and the corresponding disclination states nucleate from a round-trip resonance condition of the insulated edge state loop at the disclination polygon. To evidence the presence of disclination states and investigate their evolution when moving away from the perfect circulator condition, we represent in Fig. 1(d) the band structure of the system as a function of the circulator phase $\eta = -\xi$. The color and size of each dot is proportional to the inverse participation ratio (IPR) of the eigenstate ψ , defined as $\sum |\psi|^4 / \sum |\psi|^2$ [46]. Bulk modes, with low IPR, are in gray. As expected, when $R = 0$ ($\xi = -\eta = \pi/6$, black dashed line), one indeed observes the presence of disclination states in every anomalous gap at the expected values of $\varphi_{1/3} = \pm 0.5\pi$ (top) and $\varphi_{1/6} = \pm 0.2\pi, \pm 0.6\pi$ (bottom). When deviating from perfect circulators, we observe that the disclination states do not escape the band gaps that host them, and can be carried over to the Chern phase: they only disappear if their band gap closes, which can happen at $R = 1/3$ ($\xi = -\eta = \pi/4$, blue dashed line), i.e., at the transition between anomalous and Chern phases (see Appendices). In fact, for nonperfect circulators, the isolated disclination loop will be dispersed to generate higher-order loops “1,” “2,” and so on, based on the cycle basis in graph

theory. Concentrating on loop “1” but without loss of generality to other higher-order loops, a contrast occurs between the 1/3-cut and 1/6-cut disclination state: the former still satisfies the constructive self-interference condition at the same value of φ , which is not the case for the latter. This explains the fact that the 1/3-cut disclination state remains at a stable value of φ away from the perfect circulator condition. Contrarily, the position of the 1/6-cut disclination states shifts, while remaining inside their band gaps.

III. RELATION BETWEEN EDGE AND DISCLINATION STATES

To better highlight the connection between disclination states and topological edge states, we consider a family of finite-size scattering networks characterized by homotopy invariants associated with edge and disclination modes. The homotopy group is $\pi_1[U(N)] = \mathbb{Z}$, for mappings from the circle (spanned by a parameter k_t) to unitary matrices of dimension N , namely,

$$W[U] = \frac{1}{2\pi} \int d\phi(k_t) = \frac{1}{2\pi i} \int dk_t \text{Tr} \left(U^\dagger \frac{dU}{dk_t} \right), \quad (2)$$

where $\phi(k_t)$ is the phase of the determinant of U . In spirit, we use the fact that the sensitivity of the dynamics of the eigenenergy (quasienergy here) to changes in boundary conditions can, in principle, be used to distinguish topological states from trivial ones, whether they are bulk or states localized at an edge or disclination. We therefore associate k_t to a twisted boundary condition (TBC) implemented by nonreciprocal phase shifts added to the glued links [Fig. 2(a)]. Figure 2(b) shows the quasienergies associated with the 1/3-cut disclination states, which are the eigenphases of a 4×4 unitary operator U_d . As evident in the plot, their sum winds oppositely for edge and disclination states. Evolution of the spectrum vs k_t for (c) the edge states (zoomed in for clarity) and (d) the bulk states. In contrast, bulk states and flat bands, albeit fluctuating due to the change of the boundary condition, return to their original quasienergies without a net pump in the quasienergy spectra, therefore yielding trivial winding [$W_b = 0$, Fig. 2(d)]. This confirms that disclination states are mediated by chiral transport along the disclination loop, in a direction opposite to the outer edge states. The disclination loop therefore acts as a small hole at the center of the system, carrying topological edge states that lead to disclination states whenever a round-trip condition is met.

To complete the picture, we provide another instructive mechanism leading to the formation of disclinations. The fact that the winding invariants for disclination and edge states are opposite suggests that the disclination states may be pictured as originating from the coupling of counterpropagating chiral topological states, which is the traditional physical explanation [47] for disclinations in graphene with broken time-reversal symmetry. The topological origin of the disclination state is explained from the perspective of coupled chiral edge states and, more importantly, from the correspondence between the bound state at disclination and an additional magnetic flux localized at the disclination center. Such wedge disclinations (conical singularities) in a honeycomb lattice

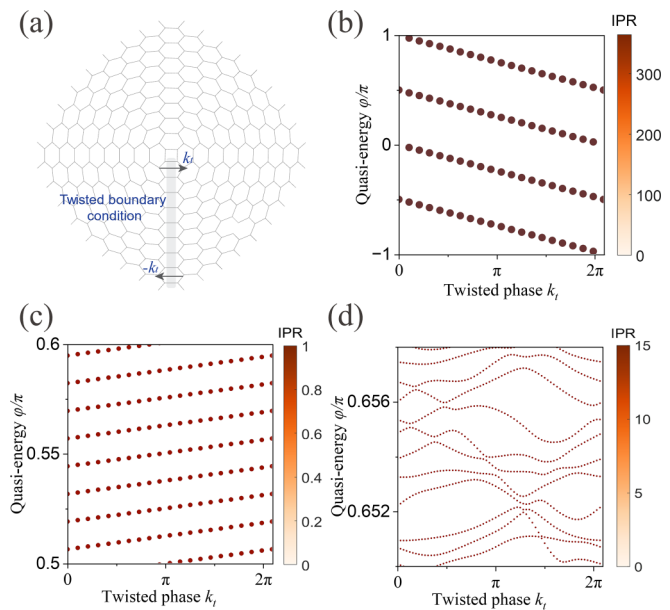


FIG. 2. Opposite quasienergy winding of edge and disclination states. A twisted boundary condition (TBC) is imparted on a cut starting from the disclination and reaching the edge of the system. This TBC introduces a nonreciprocal phase shift k_t . (b) Evolution of the disclination quasienergies vs k_t for the 1/3-cut disclination state. The sum of the quasienergies winds oppositely for edge and disclination states. Evolution of the spectrum vs k_t for (c) the edge states (zoomed in for clarity) and (d) the bulk states.

model carry an additional magnetic flux at the disclination center, which fits in to the flux pumping of electrons in a Hall cylinder. With the additional flux, eigenstates will accumulate a phase winding around the center. The correspondence between external magnetic and internal fictitious fluxes induced by wedge disclinations has an intuitive explanation via the coupling of edge modes across the seam [47,48]. Below, we use a similar description to demonstrate the origin of the disclination states by coupling chiral edge modes in our scattering network.

In order to evaluate the evolution of coupled chiral edge states and formation of disclination states when increasing the coupling strength from zero to maximum, in Fig. 3(a), we consider two independent trapezoidal networks of the same parameters (size and circulator phase). The dashed lines indicate coupling links with tunable scatterer of reflection strength θ that controls the transmission ($t = \cos \theta$) and reflection ($r = i \sin \theta$) rate through the links. A disclination state is created in the circular region. Therefore, at $\theta = 90^\circ$, the coupling links have transmission of 0 and reflection of 1, representing a zero-coupling case. There will be two independent edge states: the top trapezoidal network will have a right-propagating chiral edge state at the bottom, and the bottom trapezoidal network will have a left-propagating chiral edge state at the top. At $\theta = 0^\circ$, the coupling links have transmission of 1 and reflection of 0, and the two networks are fully connected. Figure 3(b) shows the calculated eigenmodes as a function of reflection strength θ of coupling links, focusing on the quasienergy around the disclination states. We see degenerate uncoupled edge states of each trapezoidal

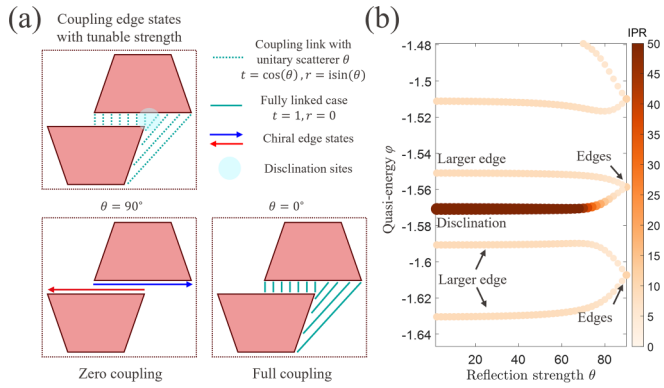


FIG. 3. Coupling chiral edge states to form a disclination. (a) Schematic of the coupling process. (b) Evolution of coupled edge states on quasienergy as a function of reflection strength.

at $\theta = 90^\circ$, and decreasing θ leads to a stronger coupling between two chiral edge states. The degeneracy is lifted to two states of distinct quasienergies. One edge state evolves into the disclination state with extremely high IPR, and the other becomes a larger edge state that winds along the two connected trapezoidal. This evolution clearly confirms the origin of the disclination state as being induced by coupling between two topological anomalous edge states. On the other hand, away from the quasienergy of the disclination state, edge states will evolve into two larger edge states. From the picture of coupled edge states, we see that the formation of a disclination state requires both a nontrivial band gap with topological edge states and the round-trip resonance condition dictated by disclination types. A closer inspection of the field distributions is made in Fig. 4 and illustrates how coupled edge states evolve into a disclination state. At state in Fig. 4(a), field distributions reveal two independent chiral edge states at each trapezoidal network (white boundaries). When coupling is turned on in Figs. 4(b)–4(d), one eigenmode features an enhanced field distribution at disclination sites (red circles), while the other features an enhanced field distribution at the larger boundary. For strong coupling in Fig. 4(d), a disclination and larger edge state are clearly observed.

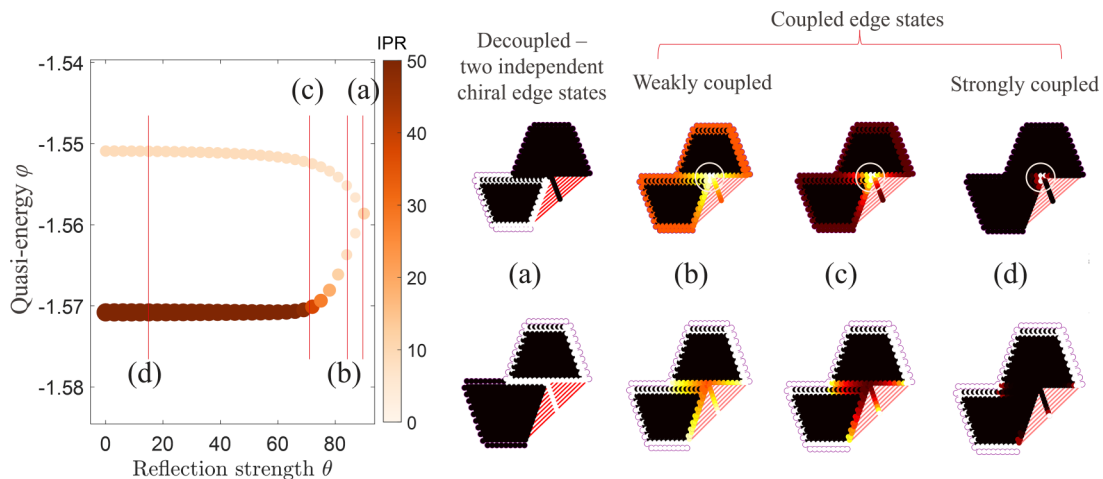


FIG. 4. Origin of disclination states from coupling counterpropagating edge states and the corresponding field distribution at four typical values: (a) $\theta = 90^\circ$, decoupled; (b) $\theta = 83^\circ$; (c) $\theta = 70^\circ$; (d) $\theta = 18^\circ$, strongly coupled.

IV. SCALING PROPERTIES

Figure 5(a) elaborates on the differences between the 0D, 1D, and bulk eigenstates of the disclinations samples. The figure focuses on a 1/3 cut in the anomalous phase. The color scale represents the IPR of the eigenstates, with darker color representing larger IPR. Disclination states have the largest IPRs and are magnified as gray dots. One finds edge states everywhere (in red), except at the location of the bulk bands (in yellow), as expected for the anomalous phase. In the Chern phase, two trivial band gaps are present, with no edge or disclination modes. We plot the spectral charge distribution for an edge state and a disclination state in Figs. 5(b) and 5(c). Both are bound states with chiral energy flow. Since now the circulators are imperfect, the disclination charges leak outward; however, an integration within the orange circle in Fig. 5(c) still yields the integer 1. Although the disclination state is intimately tied to the presence of an edge state, it is markedly different in terms of localization properties. Figure 5(d) shows the evolution of IPR for the edge state when increasing the structure’s size, which is proportional to the side length L . Conversely, for the disclination state, the IPR scales with L^2 [Fig. 5(e)], consistent with its zero-dimensional nature [49].

V. ROBUSTNESS

We now investigate the difference between Chern and anomalous disclinations, and demonstrate that the latter have superior robustness when subject to random phase disorder in the network. This constitutes a nontrivial extension of an observation already reported for topological states in codimension 1 [21,22], to 0D states in codimension 2. To evidence this, we look at the IPR of the disclination eigenmode under different strengths of quasienergy disorder. Such disorder is applied on every link between circulators, whose phase delay values are randomly drawn in the range $[\varphi_0 - \alpha/2, \varphi_0 + \alpha/2]$, with α the disorder strength. The larger the IPR, the more localized the state is, while a decrease of the IPR represents the diffusion of the disclination state energy in the network. For bulk and edge states, the IPR is near unity, but the IPR

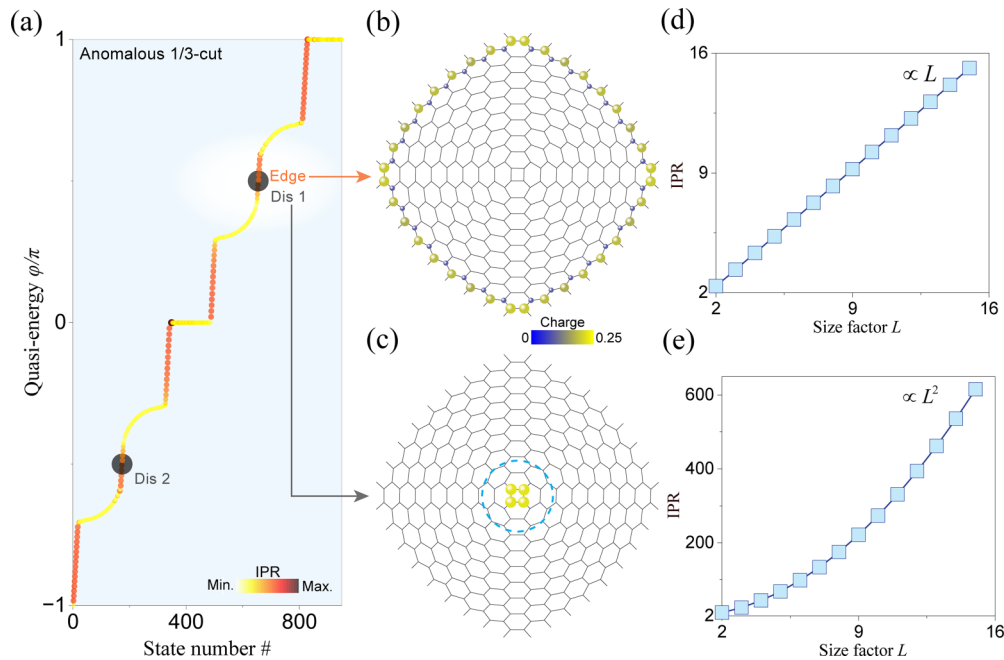


FIG. 5. Different scaling properties of the inverse participation ratios of edge and disclination states. (a) Disclination states with high IPRs can be obtained in an anomalous phase subject to a 1/3 cut. (b),(c) Focusing on the anomalous case, we plot the spectral charge distribution for (b) edge (magnified 10 times) and (c) disclination states ($\xi = -\eta = 2.5\pi/12$). Both are chiral states propagating along either the outer or the inner tetragon. (d) IPR of the 1D edge state vs system size L . (e) Same as (d) for the disclination state.

of disclination states are two orders of magnitude larger. In Fig. 6, we plot the IPRs of both anomalous and Chern disclination states, and their evolution as α is increased, averaged over 60 realizations of disorder. When $\alpha = 0$, both the anomalous and the Chern disclinations have large IPRs. However, as α increases, the Chern disclination IPR decreases drastically, whereas the anomalous one stays high. Such remarkable contrast constitutes a clear physical difference between anomalous and Chern disclinations: only the anomalous disclinations survive large distributed quasienergy disorder. Even under maximal disorder (2π phase fluctuations), the anomalous disclination states remain strongly localized. In contrast, the IPR values of the Chern disclination states are close to that of bulk states: they delocalize over

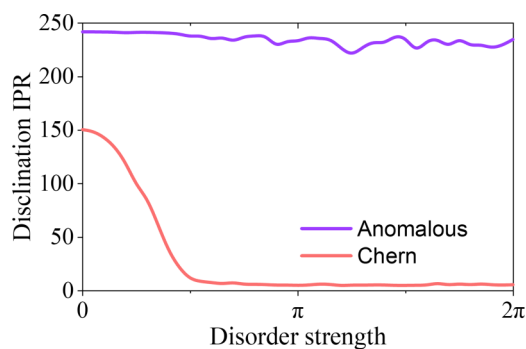


FIG. 6. Robustness of anomalous disclination states over Chern ones. The lines are obtained by averaging over 60 randomly generated realizations. The anomalous disclination IPR remains high even in the presence of random phase fluctuations, unlike the Chern one. This means that Chern disclinations delocalize easily with disorder, which is not the case for anomalous disclinations.

the entire sample. Disclination states in the anomalous phase are superiorly robust compared to those in the Chern phase because the anomalous phase has topological edge states in every band gap (no trivial band gap), while the Chern phase has a trivial band gap hosting no edge states. The trivial band gaps in the Chern phase prevent the formation of disclination states. Therefore, disclination states in the anomalous phase are robust and more bounded than in the Chern phase.

VI. DISCLINATION BICs

Can one couple anomalous chiral edge states to disclinations? The fact that anomalous disclination states coexist within a broader continuum of edge states available from external ports may be exploited to create a unique form of robust BICs in which both the bound state and the connection to the continuum are topologically chiral. By exciting the edge state from an input probe placed at the boundary [Fig. 7(a)], we can evanescently couple to the disclination state. The scattering matrix at the external probes S_{probe} is related to the internal degrees of freedom of the scattering network, and can be decomposed as [22]

$$S_{\text{probe}} = [S_{\text{ext}} + S_{\text{out}}(C_{\text{net}} - S_{\text{net}})^{-1}S_{\text{in}}], \quad (3)$$

where S_{ext} is a unitary matrix describing the direct path scattering between the probes, C_{net} is a unitary connectivity matrix describing the network, S_{net} is a unitary matrix describing the scattering inside the network, and $S_{\text{in/out}}$ are nonunitary matrices describing the coupling between the ports and the network. This equation is the scattering network equivalent of the Mahaux-Weidenmüller formula usually used to express the scattering matrix of probes in terms of a Hamiltonian description of inner dynamics [50–52]. When the matrix

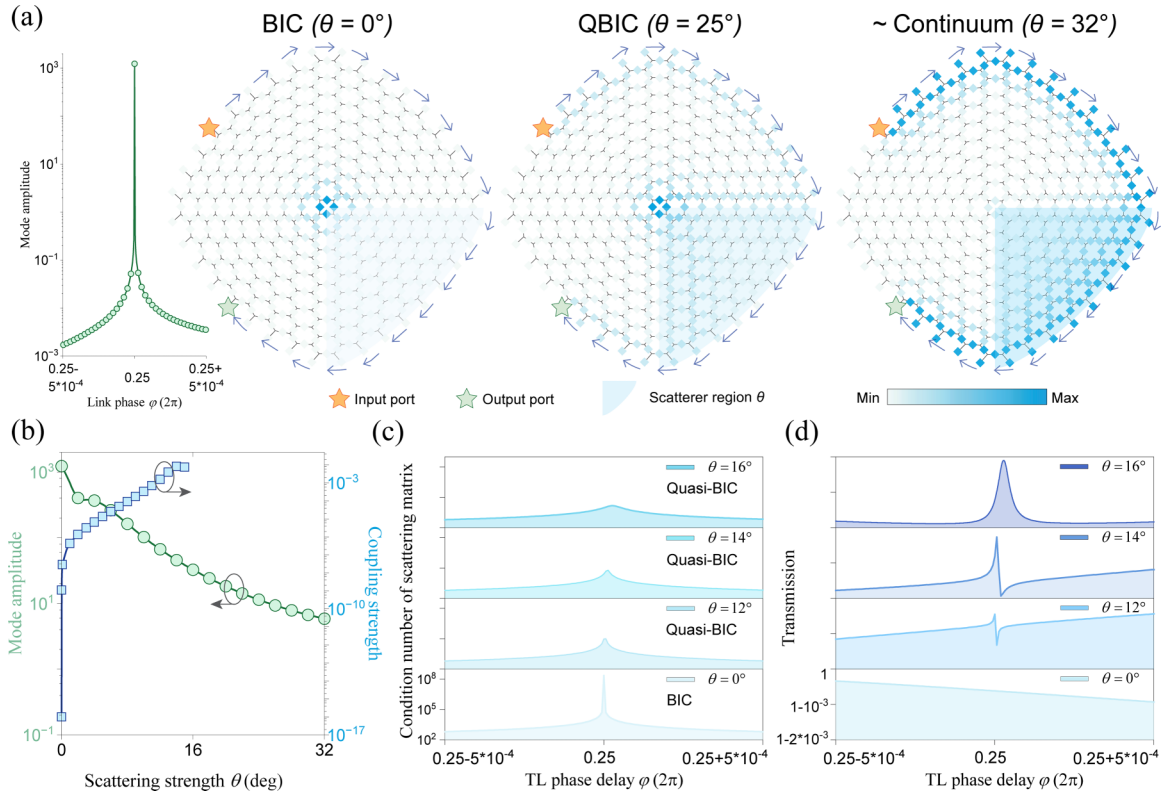


FIG. 7. Disclination bound states in a continuum in anomalous insulators. (a) Layout and field for a 1/3-cut disclination system excited from edge ports. Scatterers are added to transmission lines in a quarter region, with tunable scattering strength θ . Disclination BIC induces a greatly amplified field intensity at the disclination site (inset). Increasing θ leads to stronger coupling with the continuum, undermining the BIC to a quasi-BIC. (b) Field amplitude and edge-disclination coupling strength of the disclination BIC vs θ . Larger θ imposes stronger coupling $\langle \psi_{\text{edge}} | \psi_{\text{dis}} \rangle$ between the disclination and edge states, turning the disclination BIC into a quasi-BIC. (c) Condition number of the matrix, $C_{\text{net}} - S_{\text{net}}$, vs phase for various scattering strength θ . (d) Transmission from port 1 to port 2, confirming the vanishing linewidth associated with the BIC.

$C_{\text{net}} - S_{\text{net}}$ is not invertible, at least one inner site becomes fully disconnected and independent of the signal incident at the ports, which is the definition of a scattering network BIC. This BIC cannot couple to the continuum of topological edge states and has an infinite lifetime with large field enhancement capabilities. Figure 7(a) demonstrates a disclination BIC with remarkably enhanced field localized around the 1/3-cut disclination, when the transmission line phase is tuned to be $\varphi_{1/3} = 0.5\pi$ ($\xi = \pi/6$). A sharp peak of mode amplitude occurs under this condition when sweeping the TL phase delay (inset). The field is extremely localized with a field enhancement factor of 1250 despite lying within the continuum channel, avoiding radiation. The disclination BIC can be deteriorated by introducing a coupling mechanism with the continuum of edge states. Here, such coupling is induced by two-port scatterers at the middle of the phase links in the blue shaded area shown in Fig. 7(a). These scatterers are described by a 2×2 unitary scattering matrix with reflection coefficient $R = \sin \theta$, where θ defines a scattering strength. Tuning upward the value of θ from 0° to 32° , the BIC [left, Fig. 7(a)] transitions to a quasi-BIC [center, Fig. 7(a)], and finally merges into the continuum in the strong-coupling case [right, Fig. 7(a)]. This transition is confirmed by calculating the effective coupling strength between the disclination and the continuum, which increases from nearly zero by several orders of magnitude [blue line, Fig. 7(b)], while the mode

amplitude decreases [green line, Fig. 7(b)]. In addition, the condition number of $C_{\text{net}} - S_{\text{net}}$ in Fig. 7(c), initially infinite at $\theta = 0$, transitions to smaller values. The peak of the condition number corresponds to the peak of the mode amplitude, which confirms that BICs in a scattering network indeed arise when the matrix $C_{\text{net}} - S_{\text{net}}$ is not invertible. Sharp Fano-like signatures are obtained for quasi-BICs in the transmission spectrum measured at the output port [Fig. 7(d)], while tuning the scattering strength to zero also takes the spectral linewidth to zero, as expected for a BIC.

VII. COUPLED DISCLINATION BICs

An extended application of this disclination BIC is shown in Fig. 8. By connecting two 1/6-cut disclination networks, a y -mirror symmetric octagon is formed with two disclination sites (top and bottom disclination). By introducing coupled BICs, we reveal isolated and merged phases differing from the BIC's individual disclination charges. Near the perfect circulator condition ($\xi = -\eta = \pi/6$), the two BICs cannot couple via the central bulk and are therefore isolated, with the top disclination having a total charge of 1 and the bottom one a 0 charge, or vice versa. When deviating from this condition, a transition occurs as the two degenerate states start coupling, and they both end up with a disclination charge of 0.5, forming a merged BIC. We now start from this merged

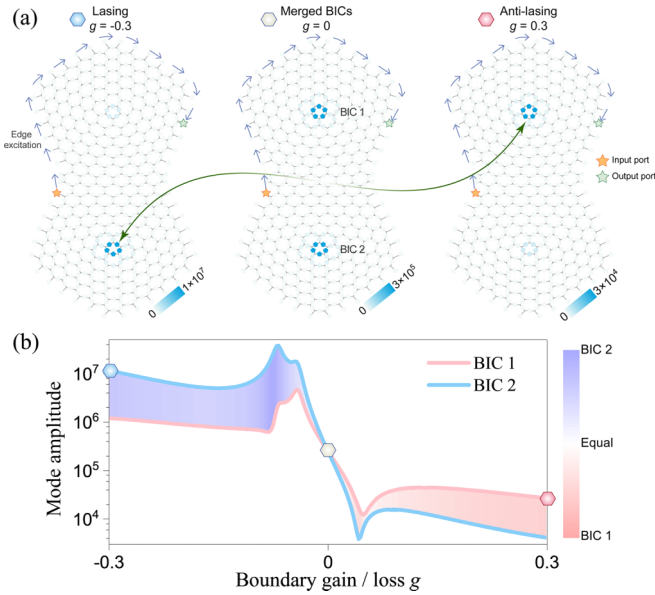


FIG. 8. Lasing-antilasing switch by topological coupling of disclination BICs. (a) Modulating gain ($g < 0$) and loss ($g > 0$) at the network boundary results in a switch between lasing and antilasing occurring when both BICs merge. In the Hermitian case ($g = 0$), the two BICs have equal intensity. (b) Evolution of the field amplitude of the two BICs when tuning g . The markers correspond to the three cases in (a).

phase, represented in Fig. 8(a), in which BICs have equal intensity, and add gain $g < 0$ or loss $g > 0$ on the boundary of the system. We see that the merged condition $g = 0$ is the transition between lasing with gain and antilasing with loss. This is confirmed by the evolution of amplitude of two BICs in Fig. 8(b). Differently, the isolated phase will enable BIC-enhanced symmetric and asymmetric lasing. The advantage of this approach is that the amplitude of the disclination BIC can be robustly amplified in both the gain and loss regions, while bringing tunability and switchability in applications including robust lasing and antilasing at topological anomalous disclination BICs. From symmetry considerations, we get two degenerate disclination states, of which we plot the individual disclination charges in Fig. 9(a) as a function of the circulator phase. Near the perfect circulator condition ($\xi = -\eta = \pi/6$), the two BICs cannot couple via the edge state and are therefore isolated, with the top disclination having a total charge of 1 and the bottom one a 0 charge, or vice versa. When deviating from this condition, a transition occurs as the two degenerate states start coupling via the chiral edge state, and they both end up with a disclination charge of 0.5, forming a merged BIC. Figure 9(c) demonstrates that the coupled disclination BICs have equal field amplitudes when merged, in contrast to the isolated BIC case with very asymmetric disclination fields. This phenomenon may be useful in lasing application: introducing gain or loss at the network boundary (parametrized by g) leads to a BIC amplitude switch happening at $g = -0.125$, in the gain region [Fig. 9(b)]. Thus, BIC-enhanced symmetric lasing can be obtained at $g = -0.125$, and lasing becomes amplitude asymmetric when deviating from this condition [Fig. 9(d)].

In conclusion, we explored the physics of disclination states in nonreciprocal topological scattering networks. Regardless of the cut-and-glue proportions, disclinations were shown to appear in a topological band gap, coexisting with anomalous chiral edge states. The disclination states were shown to survive until their band gap closes, allowing for some of these states to be carried over to the Chern phase. The relation between disclination states and topological edge states was evidenced. When they occur in the Chern phase, disclination states were shown to rapidly delocalize over the entire system under the effect of distributed quasienergy (phase) disorder. In stark contrast, anomalous disclination states survive any level of quasienergy disorder, arbitrarily larger than the band-gap size, which is a remarkable attribute of anomalous 0D disclination states. By coupling the anomalous edge state and the anomalous disclination state, we found that it was possible to form a topological nonreciprocal cavity/waveguide system where the disclination can be resonantly loaded with energy. By operating at the phase-rotation symmetry point, a singularity in the edge probe scattering matrix is induced, symptomatic of the formation of a disclination bound state embedded in the topological edge state continuum. Our study provides a different route for the exploitation of robust disclination states based on anomalous topology, in various devices and technologies, extending the reach of topological physics to sensing, signal processing, and non-Hermitian photonics.

ACKNOWLEDGMENTS

This work was supported by the Swiss State Secretariat for Education, Research and Innovation (SERI) under Contract No. MB22.00028. Z.Z. and R.F. acknowledge insightful discussions with Pierre Delplace about BICs in unitary scattering networks.

APPENDIX A: CIRCULATOR MODEL

This Appendix details the model of unitary C_3 -symmetric circulators used throughout our work. To predict the scattering of waves by a three-port circulator, one can use temporal coupled mode theory (CMT), assuming that the two dipolar modes of the ferrite cavity resonate at the eigenfrequencies ω_+ and ω_- (potentially different due to Zeeman splitting). One can couple to the two modes $|\pm\rangle$ from the external waveguides by sending a signal of complex amplitude S_i^+ at port i , and the outgoing signal at port j is noted S_j^- . The CMT equations for the amplitudes a_+ and a_- of the right-hand and left-hand modes read

$$\begin{aligned} \frac{d}{dt} a_+ &= (-i\omega_+ - \gamma_+) a_+ + \sqrt{\frac{2\gamma_+}{3}} S_1^+ \\ &\quad + e^{-i2\pi/3} \sqrt{\frac{2\gamma_+}{3}} S_2^+ + e^{-i4\pi/3} \sqrt{\frac{2\gamma_+}{3}} S_3^+, \\ \frac{d}{dt} a_- &= (-i\omega_- - \gamma_-) a_- + \sqrt{\frac{2\gamma_-}{3}} S_1^+ \\ &\quad + e^{-i2\pi/3} \sqrt{\frac{2\gamma_-}{3}} S_2^+ + e^{-i4\pi/3} \sqrt{\frac{2\gamma_-}{3}} S_3^+. \end{aligned} \quad (\text{A1})$$

The output signals S_j^- at the three ports are due to the interference between the direct reflection and the fields leaking out from each mode,

$$\begin{aligned} S_1^- &= -S_1^+ + \sqrt{\frac{2\gamma_+}{3}}a_+ + \sqrt{\frac{2\gamma_-}{3}}a_-, \\ S_2^- &= -S_2^+ + e^{i2\pi/3}\sqrt{\frac{2\gamma_+}{3}}a_+ + e^{-i2\pi/3}\sqrt{\frac{2\gamma_-}{3}}a_-, \\ S_3^- &= -S_3^+ + e^{i4\pi/3}\sqrt{\frac{2\gamma_+}{3}}a_+ + e^{-i4\pi/3}\sqrt{\frac{2\gamma_-}{3}}a_-. \end{aligned} \quad (\text{A2})$$

The overall scattering matrix of three ports can be rewritten in matrix form,

$$\begin{aligned} S_c &= -I + \kappa^2 \begin{bmatrix} \sqrt{\gamma_+} & \sqrt{\gamma_-} \\ e^{i\theta}\sqrt{\gamma_+} & e^{-i\theta}\sqrt{\gamma_-} \\ e^{i\theta}\sqrt{\gamma_+} & e^{-i\theta}\sqrt{\gamma_-} \end{bmatrix} \\ &\times \begin{bmatrix} \frac{i}{(\omega - \omega_+ + i\gamma_+)} & 0 \\ 0 & \frac{i}{(\omega - \omega_- + i\gamma_-)} \end{bmatrix} \\ &\times \begin{bmatrix} \sqrt{\gamma_+} & e^{-i\theta}\sqrt{\gamma_+} & e^{i\theta}\sqrt{\gamma_+} \\ \sqrt{\gamma_-} & e^{i\theta}\sqrt{\gamma_-} & e^{-i\theta}\sqrt{\gamma_-} \end{bmatrix}, \end{aligned} \quad (\text{A3})$$

where I is a 3×3 identity matrix, $\kappa = \sqrt{2/3}$, and $\theta = 2\pi/3$. Due to C_3 symmetry, we must have $\gamma_+ = \gamma_- = \gamma$. In order to simplify the parametrization, we transform ω_+ and ω_- into two angle variables ξ and η , by standard normalizations and arctangent transformations,

$$\xi = \arctan\left(\frac{\omega - \omega_+}{\gamma}\right), \quad \eta = \arctan\left(\frac{\omega - \omega_-}{\gamma}\right). \quad (\text{A4})$$

ξ and η are defined in $[-\pi/2, \pi/2]$ with a periodicity of π , and characterize the deviation of the angular frequency ω from the right- and left-hand eigenvalues ω_+ and ω_- , respectively. Specifically, the condition $\xi = \eta$ corresponds to the reciprocal case, with no Zeeman splitting ($\omega_+ = \omega_-$), while $\xi = -\eta$ represents the operation at the resonant frequency $\omega = \omega_0 = (\omega_+ + \omega_-)/2$, with the largest nonreciprocity. With the parameters (ξ, η) , the scattering matrix is rewritten as

$$\begin{aligned} S_c &= -I + \frac{2}{3} \begin{bmatrix} 1 & 1 \\ e^{i\frac{2\pi}{3}} & e^{-i\frac{2\pi}{3}} \\ e^{i\frac{2\pi}{3}} & e^{-i\frac{2\pi}{3}} \end{bmatrix} \\ &\times \begin{bmatrix} \cos \xi e^{i\xi} & 0 \\ 0 & \cos \eta e^{i\eta} \end{bmatrix} \\ &\times \begin{bmatrix} e^{-i\frac{2\pi}{3}} & e^{i\frac{2\pi}{3}} \\ 1 & e^{-i\frac{2\pi}{3}} \\ 1 & e^{i\frac{2\pi}{3}} \end{bmatrix}. \end{aligned} \quad (\text{A5})$$

Therefore, a general C_3 -symmetric unitary circulator is characterized by a scattering matrix $S_c = [R, T, D; D, R, T; T, D, R]$, with R, T , and D denoting the reflection and transmissions to adjacent ports, which only depend on η and ξ [21,53],

$$R = -1 + \frac{2}{3} \cos \xi e^{i\xi} + \frac{2}{3} \cos \eta e^{i\eta}, \quad (\text{A6})$$

$$T = \frac{2}{3} [e^{-i\frac{2}{3}\pi} \cos \xi e^{i\xi} + e^{i\frac{2}{3}\pi} \cos \eta e^{i\eta}], \quad (\text{A7})$$

$$D = \frac{2}{3} [e^{i\frac{2}{3}\pi} \cos \xi e^{i\xi} + e^{-i\frac{2}{3}\pi} \cos \eta e^{i\eta}]. \quad (\text{A8})$$

APPENDIX B: TOPOLOGICAL PHASE DIAGRAM OF HONEYCOMB CIRCULATOR NETWORKS

For convenience, this Appendix reproduces the topological phase diagram of circulator networks reported elsewhere [21,22]. The honeycomb network of C_3 -symmetric circulators exhibits trivial, anomalous, and Chern phases. Fixing $\xi = -\eta$ as in the main text, it is in the anomalous phase from $\xi = -\eta = 0$ to $\xi = -\eta = 3\pi/12$, and in the Chern phase from $\xi = -\eta = 3\pi/12$ to $\xi = -\eta = 6\pi/12$, with $\xi = -\eta = 3\pi/12$ the phase transition point. At $\xi = -\eta = 0$, the system becomes trivial. Circulators become perfect at $\xi = -\eta = 2\pi/12$, as shown in Figs. 10(a) and 10(b), where the transmission goes to the unity and isolation becomes infinity, indicating they are purely unidirectional. The full topological phase diagram of a honeycomb network of C_3 -symmetric circulators is shown in Fig. 11, as a function of η and ξ .

APPENDIX C: DERIVATION OF THE DISCLINATION RESONANCE CONDITION

Taking the 1/3-cut system as an example, Fig. 12 shows the derivation of Eq. (1) in the main text. At the smallest loop “0” centered at the disclination, the wave will go through four circulators [with transmission phase $\arg(T)$] and four links (with phase φ) before coming back to the start point. Therefore, for self-constructive interference, the total phase $4[\arg(T) + \varphi]$ should be a multiple of 2π . The fundamental loop “0” is dominant when circulators are around their perfect operating point ($\xi = -\eta = 2\pi/12$). Large deviation from this perfect operation point will induce strong resonance of higher-order loops such as loop “1,” “2,”.... Their resonance conditions can be similarly obtained by counting the number of circulators and phase links on the loop. A special case for 1/3-cut disclination is that high-order resonance conditions are automatically satisfied when loop “0” is resonant, leading to disclination states that do not shift in quasienergy, as reported in the main text.

APPENDIX D: EXPERIMENTAL FEASIBILITY

In this Appendix, we argue that no show-stoppers exist for the experimental observation of disclination states in such topological insulators. Hexagonal nonreciprocal networks with anomalous edge states have been experimentally realized at microwave frequencies in Refs. [21,22], and a similar experiment can be designed to probe for disclination states. Each scattering node can be implemented by commercially available surface-mount microwave circulators, and the phase

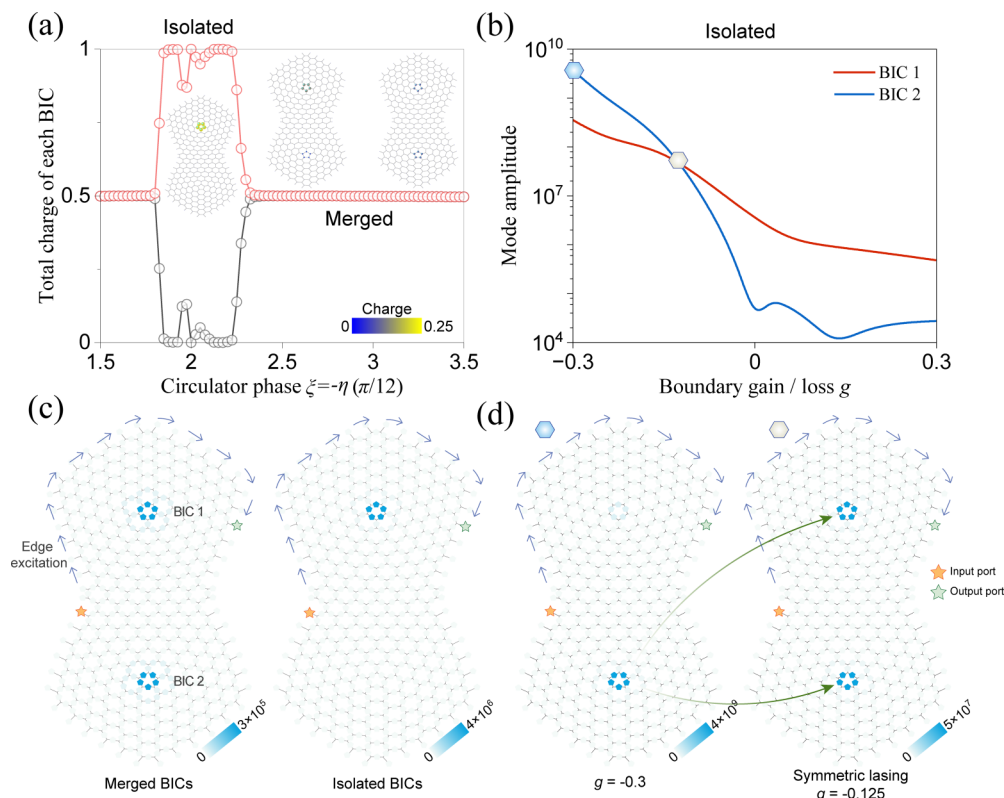


FIG. 9. Merged and isolated phase of coupled disclination BICs. (a) Evolution of total charge at two disclination sites with circulator phase in two connected 1/6-cut disclination system. There exist isolated and merged phases for coupled BICs, with the insets showing the corresponding charge distribution. (b) Modulating gain and loss at the boundary results in switch of the mode amplitude for two BICs in an isolated phase. The switch occurs in the gain regime at $g = -0.125$, indicating symmetrical lasing based on coupled BICs. (c) Coupled disclination BICs ($\xi = -\eta = 2.4\pi/12$) with equally excited BICs field at two disclination sites (left) in the merged phase and disclination BIC ($\xi = -\eta = 2.17\pi/12$) with only top site excited (right) in the isolated phase. The arrows refer to the excitation edge state for coupled disclination BICs. (d) Field profiles show asymmetric ($g = -0.3$) to symmetric ($g = -0.125$) lasing at two BICs in the isolated phase.

delay line by a simple microstrip line. The whole network is fully compatible with common fabrication methods for microwave printed circuit boards. For example, in a previous work, we have reported the real implementation of complex amorphous networks [22]. Anomalous Floquet topology even helps in this regard: it guarantees extreme robustness even in the presence of circuit flaws or badly soldered components. Also, variability in the properties of each circulator has also been shown not to be a serious issue [21], with no impact

on the topology of the anomalous phase. On a different note, adding gain or loss on the boundary of the system can be done by connecting the outer microstrip lines to low-noise

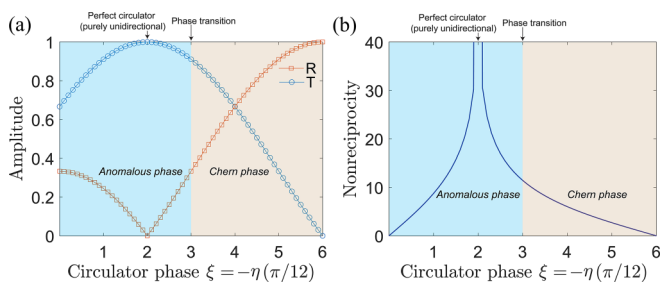


FIG. 10. (a) Example of transmission and reflection of a single circulator and (b) nonreciprocity $|T/D|$ as a function of circulator parameter $\xi = -\eta$.

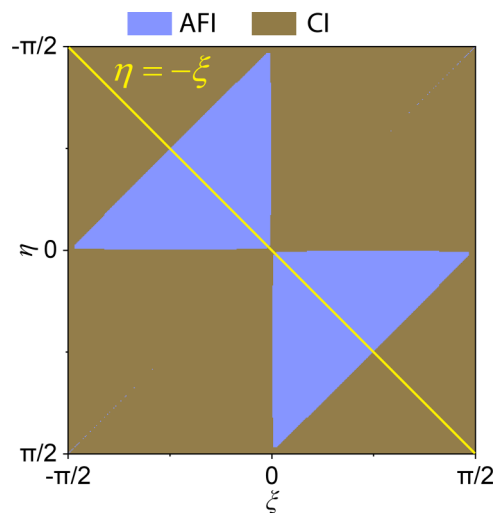


FIG. 11. Topological phase diagram as a function of circulator phases η and ξ .

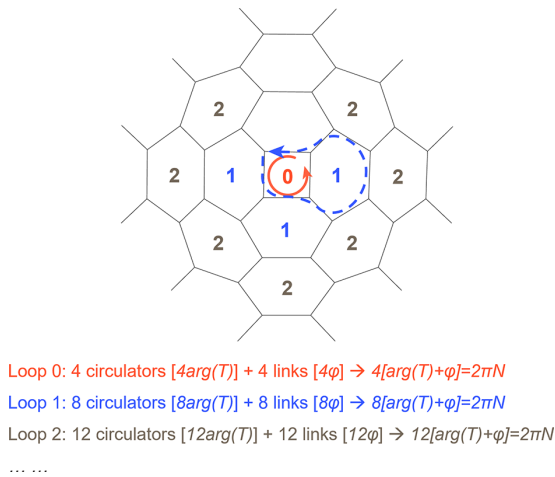


FIG. 12. Illustration of the propagation of waves in different orders of loops around a $1/3$ -cut disclination.

amplifiers (LNAs) or attenuators, which are commonly available at microwave frequencies and can be easily integrated onto the printed circuit board. The most straightforward and

clearest physical observable for confirming the presence of the disclination state is a field map measurement. This can be obtained from a field scanning experiment performed with a local probe exciting the disclination center, as typically done for corner states. The field map can be extracted by exciting the network in the near field with a coaxial probe connected to port 1, and manually probing the field at the middle of the microstrip lines by using another coaxial probe, which is connected to port 2. The other way is through a measurement of the BIC line shape (Fig. 7). Since the disclination state is a bound state, we can excite from the boundary of the network due to the weak coupling between the disclination and edge state. A quasi-BIC should show up as a very sharp signature in the edge-state transmission or reflection spectra. Finally, to characterize the topology of the disclination state, the twisted boundary condition can also be experimentally realized, as in [22]. By tuning the twisted phase during a circle ($0 \sim 2\pi$), the quasienergy should wind by 2π and reveal the topological nature of the disclination state. Such winding must translate into observable frequency shifts of the disclination resonance frequencies, which can be measured by looking at the reflection spectrum of a near-field coupled probe near the disclination center.

-
- [1] X.-L. Qi and S.-C. Zhang, Topological insulators and superconductors, *Rev. Mod. Phys.* **83**, 1057 (2011).
- [2] M. Z. Hasan and C. L. Kane, Colloquium: Topological insulators, *Rev. Mod. Phys.* **82**, 3045 (2010).
- [3] N. A. Olekhno, E. I. Kretov, A. A. Stepanenko, P. A. Ivanova, V. V. Yaroshenko, E. M. Puhtina, D. S. Filonov, B. Cappello, L. Matekovits, and M. A. Gorlach, Topological edge states of interacting photon pairs emulated in a topoelectrical circuit, *Nat. Commun.* **11**, 1436 (2020).
- [4] L. Lu, J. D. Joannopoulos, and M. Soljačić, Topological photonics, *Nat. Photon.* **8**, 821 (2014).
- [5] C. He, X. Ni, H. Ge, X.-C. Sun, Y.-B. Chen, M.-H. Lu, X.-P. Liu, and Y.-F. Chen, Acoustic topological insulator and robust one-way sound transport, *Nat. Phys.* **12**, 1124 (2016).
- [6] H. Xue, Y. Yang, F. Gao, Y. Chong, and B. Zhang, Acoustic higher-order topological insulator on a kagome lattice, *Nat. Mater.* **18**, 108 (2019).
- [7] F. D. M. Haldane, Model for a quantum Hall effect without Landau levels: Condensed-matter realization of the “parity anomaly”, *Phys. Rev. Lett.* **61**, 2015 (1988).
- [8] G. Chen, A. L. Sharpe, E. J. Fox, Y.-H. Zhang, S. Wang, L. Jiang, B. Lyu, H. Li, K. Watanabe, T. Taniguchi, Z. Shi, T. Senthil, D. Goldhaber-Gordon, Y. Zhang, and F. Wang, Tunable correlated Chern insulator and ferromagnetism in a moiré superlattice, *Nature (London)* **579**, 56 (2020).
- [9] Z. Wang, Y. Chong, J. D. Joannopoulos, and M. Soljačić, Observation of unidirectional backscattering-immune topological electromagnetic states, *Nature (London)* **461**, 772 (2009).
- [10] Y. Ding, Y. Peng, Y. Zhu, X. Fan, J. Yang, B. Liang, X. Zhu, X. Wan, and J. Cheng, Experimental demonstration of acoustic Chern insulators, *Phys. Rev. Lett.* **122**, 014302 (2019).
- [11] M. S. Rudner, N. H. Lindner, E. Berg, and M. Levin, Anomalous edge states and the bulk-edge correspondence for periodically driven two-dimensional systems, *Phys. Rev. X* **3**, 031005 (2013).
- [12] Y.-G. Peng, C.-Z. Qin, D.-G. Zhao, Y.-X. Shen, X.-Y. Xu, M. Bao, H. Jia, and X.-F. Zhu, Experimental demonstration of anomalous Floquet topological insulator for sound, *Nat. Commun.* **7**, 13368 (2016).
- [13] G. G. Pyrialakos, J. Beck, M. Heinrich, L. J. Maczewsky, N. V. Kantartzis, M. Khajavikhan, A. Szameit, and D. N. Christodoulides, Bimorphic Floquet topological insulators, *Nat. Mater.* **21**, 634 (2022).
- [14] K. Wintersperger, C. Braun, F. N. Ünal, A. Eckardt, M. D. Liberto, N. Goldman, I. Bloch, and M. Aidelsburger, Realization of an anomalous Floquet topological system with ultracold atoms, *Nat. Phys.* **16**, 1058 (2020).
- [15] M. Pasek and Y. D. Chong, Network models of photonic Floquet topological insulators, *Phys. Rev. B* **89**, 075113 (2014).
- [16] P. Delplace, M. Fruchart, and C. Tauber, Phase rotation symmetry and the topology of oriented scattering networks, *Phys. Rev. B* **95**, 205413 (2017).
- [17] L. J. Maczewsky, J. M. Zeuner, S. Nolte, and A. Szameit, Observation of photonic anomalous Floquet topological insulators, *Nat. Commun.* **8**, 13756 (2017).
- [18] S. Mukherjee, A. Spracklen, M. Valiente, E. Andersson, P. Öhberg, N. Goldman, and R. R. Thomson, Experimental observation of anomalous topological edge modes in a slowly driven photonic lattice, *Nat. Commun.* **8**, 13918 (2017).
- [19] S. Afzal, T. J. Zimmerling, Y. Ren, D. Perron, and V. Van, Realization of anomalous Floquet insulators in strongly coupled nanophotonic lattices, *Phys. Rev. Lett.* **124**, 253601 (2020).
- [20] H. Zhong, Y. V. Kartashov, Y. Li, and Y. Zhang, π -mode solitons in photonic Floquet lattices, *Phys. Rev. A* **107**, L021502 (2023).

- [21] Z. Zhang, P. Delplace, and R. Fleury, Superior robustness of anomalous non-reciprocal topological edge states, *Nature (London)* **598**, 293 (2021).
- [22] Z. Zhang, P. Delplace, and R. Fleury, Anomalous topological waves in strongly amorphous scattering networks, *Sci. Adv.* **9**, eadg3186 (2023).
- [23] M. Li, D. Zhirihin, M. Gorlach, X. Ni, D. Filonov, A. Slobozhanyuk, A. Alú, and A. B. Khanikaev, Higher-order topological states in photonic kagome crystals with long-range interactions, *Nat. Photon.* **14**, 89 (2020).
- [24] X. Ni, M. Weiner, A. Alú, and A. B. Khanikaev, Observation of higher-order topological acoustic states protected by generalized chiral symmetry, *Nat. Mater.* **18**, 113 (2019).
- [25] Y. Liu, S. Leung, F.-F. Li, Z.-K. Lin, X. Tao, Y. Poo, and J.-H. Jiang, Bulk-disclination correspondence in topological crystalline insulators, *Nature (London)* **589**, 381 (2021).
- [26] Y. Chen, Y. Yin, Z.-K. Lin, Z.-H. Zheng, Y. Liu, J. Li, J.-H. Jiang, and H. Chen, Observation of topological p -orbital disclination states in non-Euclidean acoustic metamaterials, *Phys. Rev. Lett.* **129**, 154301 (2022).
- [27] Y. Deng, W. A. Benalcazar, Z.-G. Chen, M. Oudich, G. Ma, and Y. Jing, Observation of degenerate zero-energy topological states at disclinations in an acoustic lattice, *Phys. Rev. Lett.* **128**, 174301 (2022).
- [28] C. W. Peterson, T. Li, W. Jiang, T. L. Hughes, and G. Bahl, Trapped fractional charges at bulk defects in topological insulators, *Nature (London)* **589**, 376 (2021).
- [29] W. A. Benalcazar and A. Cerjan, Bound states in the continuum of higher-order topological insulators, *Phys. Rev. B* **101**, 161116(R) (2020).
- [30] A. Cerjan, M. Jürgensen, W. A. Benalcazar, S. Mukherjee, and M. C. Rechtsman, Observation of a higher-order topological bound state in the continuum, *Phys. Rev. Lett.* **125**, 213901 (2020).
- [31] Z. Hu, D. Bongiovanni, D. Jukić, E. Jajtić, S. Xia, D. Song, J. Xu, R. Morandotti, H. Buljan, and Z. Chen, Nonlinear control of photonic higher-order topological bound states in the continuum, *Light Sci. Appl.* **10**, 164 (2021).
- [32] R.-J. Slager, The translational side of topological band insulators, *J. Phys. Chem. SolidsSpin-Orbit Coupl. Mater.* **128**, 24 (2019).
- [33] M. S. Kirsch, Y. Zhang, M. Kremer, L. J. Maczewsky, S. K. Ivanov, Y. V. Kartashov, L. Torner, D. Bauer, A. Szameit, and M. Heinrich, Nonlinear second-order photonic topological insulators, *Nat. Phys.* **17**, 995 (2021).
- [34] B. Ren, H. Wang, Y. V. Kartashov, Y. Li, and Y. Zhang, Nonlinear photonic disclination states, *APL Photon.* **8**, 016101 (2023).
- [35] T. Nag and B. Roy, Anomalous and normal dislocation modes in Floquet topological insulators, *Commun. Phys.* **4**, 157 (2021).
- [36] D. J. Salib and B. Roy, Dynamic metal along grain boundaries in Floquet topological crystals, [arXiv:2212.08060](https://arxiv.org/abs/2212.08060).
- [37] F. Schindler, A. M. Cook, M. G. Vergniory, Z. Wang, S. S. P. Parkin, B. A. Bernevig, and T. Neupert, Higher-order topological insulators, *Sci. Adv.* **4**, eaat0346 (2018).
- [38] W. A. Benalcazar, B. A. Bernevig, and T. L. Hughes, Quantized electric multipole insulators, *Science* **357**, 61 (2017).
- [39] B. Bahari, A. Ndao, F. Vallini, A. El Amili, Y. Fainman, and B. Kanté, Nonreciprocal lasing in topological cavities of arbitrary geometries, *Science* **358**, 636 (2017).
- [40] Y. Ota, K. Takata, T. Ozawa, A. Amo, Z. Jia, B. Kante, M. Notomi, Y. Arakawa, and S. Iwamoto, Active topological photonics, *Nanophotonics* **9**, 547 (2020).
- [41] P. St-Jean, V. Goblot, E. Galopin, A. Lemaître, T. Ozawa, L. Le Gratiet, I. Sagnes, J. Bloch, and A. Amo, Lasing in topological edge states of a one-dimensional lattice, *Nat. Photon.* **11**, 651 (2017).
- [42] G. Harari, M. A. Bandres, Y. Lumer, M. C. Rechtsman, Y. D. Chong, M. Khajavikhan, D. N. Christodoulides, and M. Segev, Topological insulator laser: Theory, *Science* **359**, eaar4003 (2018).
- [43] M. A. Bandres, S. Wittek, G. Harari, M. Parto, J. Ren, M. Segev, D. N. Christodoulides, and M. Khajavikhan, Topological insulator laser: Experiments, *Science* **359**, eaar4005 (2018).
- [44] H.-R. Kim, M.-S. Hwang, D. Smirnova, K.-Y. Jeong, Y. Kivshar, and H.-G. Park, Multipolar lasing modes from topological corner states, *Nat. Commun.* **11**, 5758 (2020).
- [45] H. Zhong, Y. V. Kartashov, A. Szameit, Y. Li, C. Liu, and Y. Zhang, Theory of topological corner state laser in kagome waveguide arrays, *APL Photon.* **6**, 040802 (2021).
- [46] D. J. Thouless, Electrons in disordered systems and the theory of localization, *Phys. Rep.* **13**, 93 (1974).
- [47] A. Rüegg and C. Lin, Bound states of conical singularities in graphene-based topological insulators, *Phys. Rev. Lett.* **110**, 046401 (2013).
- [48] Y.-Q. Wang and J. E. Moore, Boundary edge networks induced by bulk topology, *Phys. Rev. B* **99**, 155102 (2019).
- [49] G. A. Domínguez-Castro and R. Paredes, The Aubry-André model as a hobbyhorse for understanding the localization phenomenon, *Eur. J. Phys.* **40**, 045403 (2019).
- [50] Mahaux and H. A. Weidenmüller, *Shell-Model Approach to Nuclear Reactions*, (North-Holland, Amsterdam, 1969).
- [51] H.-G. Zirnstein, G. Refael, and B. Rosenow, Bulk-boundary correspondence for non-Hermitian Hamiltonians via Green functions, *Phys. Rev. Lett.* **126**, 216407 (2021).
- [52] D. S. Borgnia, A. J. Kruchkov, and R.-J. Slager, Non-Hermitian boundary modes and topology, *Phys. Rev. Lett.* **124**, 056802 (2020).
- [53] A. B. Khanikaev, R. Fleury, S. H. Mousavi, and A. Alú, Topologically robust sound propagation in an angular-momentum-biased graphenelike resonator lattice, *Nat. Commun.* **6**, 8260 (2015).